Nanoscale

Accepted Manuscript

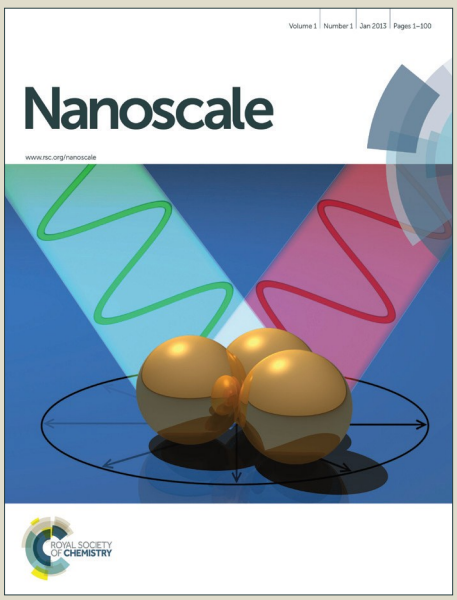

ROYAL SOCIETY OF CHEMISTRY

www.rsc.org/nanoscale

TiC_2: A New Two-Dimensional Sheet beyond MXenes

Tianshan Zhao,[a,b] Shunhong Zhang,[a,b] Yaguang Guo,[a,b] and Qian Wang[*a,b]

[a] Center for Applied Physics and Technology, College of Engineering, Peking University, Beijing 100871, China

[b]IFSA Collaborative Innovation Center, and Key Laboratory of High Energy Density Physics Simulation, Ministry of Education, Beijing 100871, China

*E-mail: qianwang2@pku.edu.cn

Abstract

MXenes are attracting attention due to their rich chemistry and intriguing properties. Here a new type of metal-carbon-based sheet composed of transition metal centers and C_2 dimers rather than individual C atoms is designed. Taking the Ti system as a test case, density functional theory calculations combined with a thermodynamic analysis uncover the thermal and dynamic stability of the sheet, as well as a metallic band structure, anisotropic Young's modulus and Poisson's ratio, a high heat capacity, and a large Debye stiffness. Moreover, the TiC_2 sheet has excellent Li storage capacity with a small migration barrier, a lower mass density compared with standard MXenes, and better chemical stability as compared to the MXene Ti_2C sheet. When Ti is replaced with other transition metal centers, diverse new MC_2 sheets containing C=C dimers can be formed, the properties of which merit further investigation.

Introduction

Carbon, due to its unique flexibility to manipulate its four valence electrons in very flexible ways, forms diverse allotropes ranging from the well-known graphite and diamond to more recent C_{60} fullerene, nanotube, nanochain, and to the newly discovered two-dimensional (2D) carbon like graphene,[1] graphyne,[2] graphdiyne,[2] and penta-graphene.[3] The unusual mechanical, electronic, optical, catalytic, and transport properties of these 2D carbon systems and their numerous technological applications have led to considerable interest in the study of other C-based 2D materials. One such example is the hotly pursued MXene type $M_{n+1}C_n$ layers,[4-7] a group of 2D early transition metal (TM) carbides derived from chemical exfoliation of the MAX phases, where the concentration of transition metal atoms (including Sc, Ti, V, Cr, Zr, Zb, Mo, Hf and Ta) exceeds that of carbon, and carbon is atomically bonded to metal atoms. Because of their rich structural chemistry and good electronic conductivity, MXenes are promising candidates for applications in sensors, electronic devices, catalysts, conductive reinforcement additives to polymers, and electrochemical energy storage or conversion materials.[8, 9] However, the main disadvantage of MXenes is that the metal atoms are highly exposed on the surfaces. In addition, the surface functionalization is needed for applications in many cases.[8, 10] Thus, it is necessary to go beyond the morphology of MXenes to design a new type of metal carbide sheet where metal atoms are less than carbon and carbon is bonded molecularly rather than atomically with metal atoms. Such kind of sheets can not only reduce their mass density and exposed metal sites with improved chemical stability, but also have different properties due to the change of binding mode.

In fact, C_2 dimer is the basic structural unit in the growth of many carbon structures such as fullerenes, nanotube, graphene, and graphyne,[2, 11-14] and even emerges on the reconstructed diamond surface.[15] C_2 is also the building unit of diverse carbon compounds such as metallocarbohedrenes (Met-Cars) M_mC_n,[16, 17] metal-alkynide complexes,[18] alkynide complexes,[19] organic materials,[20] and some binary or ternary metal carbides ($LiAgC_2$, $KAgC_2$,

$CsAgC_2$ and $NaPdC_2$).[21, 22] The first member of the Met-Cars family, Ti_8C_{12}, was discovered in 1992 by the Castleman group,[16] then the other members, M_8C_{12} with M=Sc, Zr, Hf, V, Nb, Ta, Cr, Mo, and Fe, were also synthesized[23, 24] and joined in the family soon afterward. The common structural feature of these Met-Cars is that the six C_2 dimers are connected by eight TM atoms, forming cage-like structures. In addition, C_2 molecule is a well-known pseudo-oxygen unit with an electron affinity (EA) of 3.4 eV which is nearly three times as large as that of a carbon atom. It has been demonstrated that C_2 dimers play a key role in the stability during the growth of Met-Cars where the clusters containing C_2 dimers are energetically more favorable than structures containing only individual carbon atoms or trimers.[25] More interestingly, C_2 dimers are also found to exist in both low and high carbon steels.[26, 27]

Despite the versatility of C_2 dimer in forming diverse structures, there has been no report to date on a 2D crystal that consists of transition metal atoms and C_2 dimers. In MXenes[4, 8] and other theoretically predicted metal carbide sheets,[28] carbon atoms bind to metal atoms individually. Here we present a comprehensive theoretical study of a 2D sheet composed of transition metal centers and C_2 dimers by taking the Ti system as an example. The calculated results reveal that the TiC_2 sheet is not only stable dynamically and thermally, but also it is metallic with outstanding Li storage capacity beyond existing MXene Ti_2C layers. Like MXene Ti_2C, the Ti in TiC_2 could also be replaced with other transition metal elements, thus giving rise to a new type of 2D metal carbides MC_2 with exceptional properties.

Computational methords

Atomic structure optimizations and electronic structure calculations are carried out using density functional theory (DFT) as implemented in the Vienna *Ab initio* Simulation Package (VASP).[27] The projector augmented wave (PAW) method[29] and Perdew-Burke-Ernzerhof (PBE) exchange correlation functional within generalized gradient approximation (GGA)[30] are used. The $2s^1$, $2s^2 2p^2$ and $3d^3 4s^1$ atomic orbitals are treated as valence states for Li, C, and

Ti, respectively. Plane waves with kinetic energy cutoff of 500 eV are used to expand the valence electron wave functions. For all structural relaxations the convergence criteria for total energy and Hellmann-Feynman force are set to be 10^{-4} eV and 10^{-2} eV/Å, respectively. A unit cell with a vacuum space of 20 Å in the direction perpendicular to the nanosheet is used in order to avoid virtual interactions. The first Brillouin zone is sampled by a 7×7×1 k-point grid within the Monkhorst-Pack scheme.[31] To check the dynamic stability, we use density functional perturbation theory (DFPT) to calculate the force constants. The Phonopy code[32] is used to calculate the vibrational spectra. *Ab initio* molecular dynamics (AIMD) simulations are also performed to assess the thermal stability of the TiC_2 sheet. Canonical (NVT) ensemble is adopted using the Nosé heatbath method.[33] Bader charge analysis[34] is carried out to study the charge distribution and transfer quantitatively. By using the nudged elastic band (NEB) method,[35] we calculate the diffusion energy barrier and the minimum energy pathway of Li diffusion on the TiC_2 sheet.

Results and discussion

1. Geometry and Stability

The most well-known carbon-metal nanostructure containing C_2 units is the Ti_8C_{12} Met-Car that was initially suggested to have T_h symmetry where the 20 atoms forms a nearly regular pentagonal dodecahedron,[16, 17] as shown in Fig. 1a. However, the Ti_8C_{12} all-pentagon cage structure was later found to be unstable and transform to a C_{3v}-like structure[17] (Fig. 1b). Rohmer *et al.*[36] analyzed the all possible structures of the Ti_8C_{12} cluster, and found that the 8 Ti atoms forms a pseudocubic framework, each C_2 unit could be oriented along one or other diagonal of the underlying face of the pseudocubic framework, independent of other dicarbon fragments. Following such an idea, we use a planar triangular Ti lattice like the first layer of (0001) surface of *hcp* bulk Ti, and build a 2D Ti-C sheet by depositing C_2 dimers on the surface with different positions and orientations, yielding three candidate structures with a

chemical formula TiC_2, as shown in Fig. S1. It is interesting to note that the most stable configuration (Fig. 1d) has the same geometry as optimized from penta-graphene like structure (Fig. 1c). Different from MXenes,[4, 9, 10, 37] in the stable TiC_2 sheet, Ti atoms are sandwiched between the top and bottom C_2 layers, leading to a quasi-2D sheet with no exposed Ti atoms on the surfaces. Another difference between TiC_2 and the MXenes layers is that in MXenes, carbon atoms are atomically bonded to its neighboring TM atoms with the C-C distance in the range of 2.80 to 3.35 Å,[4, 9, 11, 38] while the C-C distance in TiC_2 is only 1.33 Å, showing a double bond character,[39] and implying that the carbon atoms exist in the form of C_2 dimer. In addition, unlike MXenes that have hexagonal symmetry,[4] TiC_2 has a rectangular lattice with the optimized lattice parameters of a = 4.96 Å and b = 3.59 Å. The C-C bond in TiC_2 is also stronger than that in the dodecahedral Ti_8C_{12} cage where the C-C bond length is 1.40 Å,[16] and is comparable to that in the C_{3v} -like structure (1.34 Å).[17] Note that in bulk metal carbides the C-C bond can vary from conventional single bonds to typical triple bonds.[39]

To study possible reasons why the structures in Fig. 1a and 1c are less stable than those in Fig. 1b and 1d, respectively, we have carefully checked their bonding features and found that in the T_h cage structure, all C_2 dimers bind with Ti atoms in end-on configuration (EOC),[40] while in the C_{3v}-like structure[41] besides the EOC binding for some Ti atoms (labeled as Ti_1 in Fig. 1b), C_2 dimers also bind with Ti in side-on configuration (SOC) (labeled such Ti atoms as Ti_2). Similarly, the pentagon based sheet (Fig. 1c) only contains the EOC binding mode, while the three-atomic-layer sheet (Fig. 1d) has both the EOC and SOC binding modes. The corresponding Ti-C bond length in the EOC and SOC modes is 2.05 Å and 2.20 Å, respectively, close to the that of 2.10 Å in Ti_2C MXene monolayer.[42] In fact, it has been demonstrated experimentally and theoretically that the SOC binding mode is more energetically favorable over the EOC mode in Met-Car structures.[17, 36, 43-45] Therefore, containing the SOC binding mode is the possible reason why the C_{3v}-like structure is more

stable than the pentagonal dodecahedron as is also the case with the TiC_2 sheet adopted the configuration containing the SOC mode. The simulated Scanning Tunneling Microscopy (STM) (using the constant height model[46] with a height of 0.9 Å and a negative bias of 0.05 V) and Transmission Electron Microscopy (TEM)[47, 48] (base on the so-called independent atom model which is also called procrystal model[49]) images of the optimized TiC_2 sheet are given in Fig. 1e and 1f for the convenience of comparison with experimental results in the future.

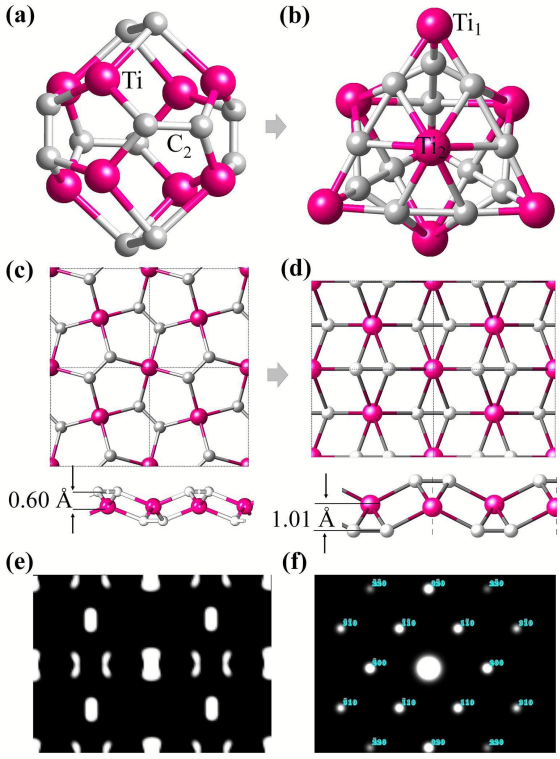

Fig. 1 (a) Dodecahedral configuration of the Ti_8C_{12} cage with T_h symmetry. (b) Ground state configuration of the T_8C_{12} cage with C_{3v} symmetry. Ti_1 and Ti_2 refer to the Ti atoms with the SOC and EOC binding modes, respectively. (c) An all-pentagon TiC_2 sheet derived from penta-graphene. (d) Optimized structure of the TiC_2 sheet starting from the structure in (c). (e) and (f) Simulated STM and TEM images of the optimized TiC_2 sheet, respectively.

The thermodynamic stability of the 2D TiC_2 structure was studied by carrying out additional calculations with many other possible structural isomers. For instance, two energetically low-lying isomers are given in Fig. S2a and S2b, which are also composed of C_2 units and Ti atoms with square and rectangle lattices, respectively. The former one contains both the EOC and SOC binding modes, while the latter has the EOC mode only. The optimized structures are given in Fig. S2c and S2d. Total energy calculations show that these two structures are respectively 0.75 and 0.78 eV per formula unit (f. u.) higher in energy than the structure given in Fig. 1d. The underlying reason is that the binding mode is different in these three configurations. In Fig. S2d, the binding between the Ti and C_2 units is EOC only, while in Fig. S2c, although the SOC binding mode also exists, the two neighboring C_2 units are perpendicular to each other, which also differ from the parallel alignment of C_2 units in Fig. 1d. Thus, the resulting stresses make the two structures energetically unfavorable as compared to the one shown in Fig. 1d. We also compare the thermodynamic stability of the TiC_2 sheet with some previously identified Ti-C compounds with other stoichiometry. Detailed discussions can be found in the Supplementary Information.

We now focus on the energetically most stable structure of the TiC_2 sheet. The phonon frequencies and phonon density of states (DOS) are calculated with high accuracy to examine its dynamical stability. The calculated results are summarized in Fig. 2, which shows that the TiC_2 sheet is dynamically stable as no imaginary frequencies exist in the entire Brillouin Zone. The vibrational modes below 350 cm^{-1} including the three acoustic bands and three optical bands are mainly contributed by Ti due to its larger atomic mass.[50] The two highest optical modes are separated from others by a large phonon gap of around 800 cm^{-1}. Comparing the peaks of phonon PDOS with the phonon bands, the following features are identified: the *z* direction displacement pattern of Ti atoms (Ti_z) contributes to the *z* direction acoustic branch (ZA), the *y* direction displacement pattern (Ti_y) constitutes the transverse acoustic branch (TA), and the longitudinal acoustic (LA) branch is formed by the displacement of Ti along the

x direction (Ti_x). The C_y and C_z vibrations make main contributions to the optical bands between 350 cm^{-1} and 650 cm^{-1}. The stretching mode of the C=C bonds (C_x) corresponds to the two highest optical branches. The highest optical mode reaches up to 1600 cm^{-1}, which is comparable to that of the C=C bonds in recently reported carbon structures,[3, 51] but it is higher than that of Ti_8C_{12} cluster (1360 cm^{-1})[52] due to the different bond orders.

To study the thermal stability of the TiC_2 sheet at finite temperature, we perform AIMD simulations at 350 K using a relatively large (4×4) supercell as a small unit cell may easily result in false instability. The time step is set as 1 femtosecond (*fs*). After 5 picoseconds of simulation, no structural distortion or reconstruction is found, and the average total potential energy remains nearly constant as shown in Fig. S5, confirming that TiC_2 is thermally stable at room temperature. The thermal stability of TiC_2 provides the possibility of its future synthesis and application at ambient conditions.

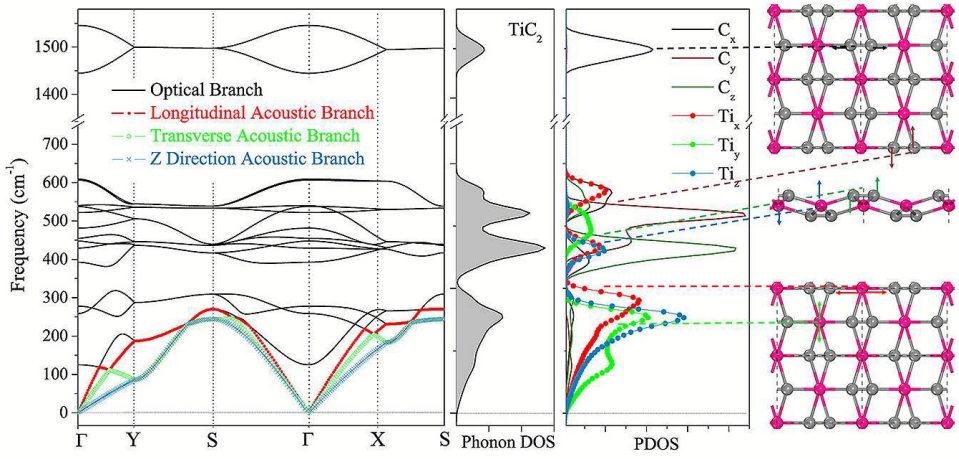

Fig. 2. Phonon dispersion, and total and partial phonon DOS of the TiC_2 sheet. Some characteristic vibrational modes are indicated in the most right column.

2. Thermodynamic Properties

Based on the calculated phonon spectrum, a series of thermodynamic properties can be derived. Here we concentrate on studies of the heat capacity and Debye temperature of the

TiC_2 sheet. The calculated phonon heat capacity with respect to temperature is plotted in Fig. 3a. The heat capacity can also be expressed using the phonon DOS[53] The Debye temperature $\Theta_D=h\nu_D/k_B$ is determined by fitting the calculated C_V-T curve using Debye model. The fitted Debye temperature $\Theta_D(T)$ is given in Fig. 3b, which shows that the $\Theta_D(T)$ is as high as 850 K at room temperature. Since the vibrational frequency is proportional to the square root of the stiffness within the harmonic approximation, Θ_D can be used as a measurement of the "stiffness" of solids.[53] Therefore, from Fig. 3b we see that the TiC_2 sheet can display large Debye stiffness due to its high Debye temperature, resulting from the covalent C=C bonds.

As phonons are subjected to Bose-Einstein distribution, the weighted phonon DOS $g(\nu)\,\mathrm{W}(h\nu/k_BT)$ describes the contribution of vibrational modes with certain frequency to the heat capacity. The frequency and temperature dependence of the weighted phonon DOS is plotted in Fig. 3c. We find that at 50 K, only about 2.5 % or even less weighting factor W ($h\nu/k_BT$) exists in the frequency region over 400 cm^{-1}, indicating that only low-frequency states contribute to the heat capacity at low temperature. This is evidenced by Fig. 3d showing the variation of the weighted phonon DOS with respect to frequency at different temperatures. Since the heat capacity defined by Debye model is proportional to the cross section of *Frequency-Phonon DOS* at a given temperature, a larger amount of heat is required to increase the temperature by one Kalvin when the cross section is larger. Because TiC_2 has more vibrational states than graphite and diamond[53] in the low frequency region, TiC_2 exhibits larger heat capacity under 350 K.

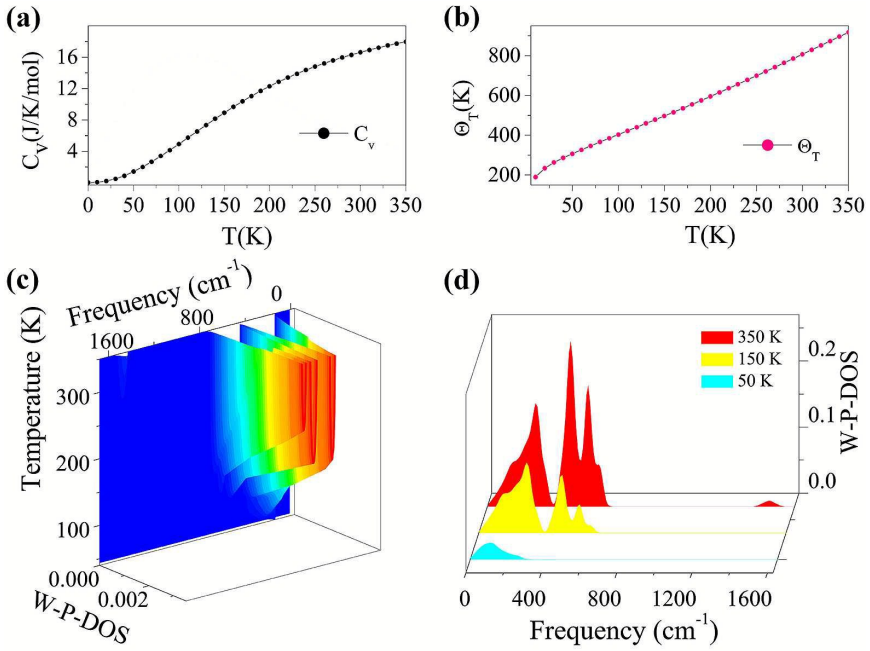

Fig. 3 (a) Heat capacity, and (b) Debye temperature with respect to temperature of the TiC2 sheet; (c) 3D plot of the weighted phonon DOS (W-P-DOS) as the function of frequency and temperature; (d) Cross sections of the W-P-DOS at 50, 150 and 350 K.

3. Mechanical Properties

To further investigate how lattice distortions affect the structural stability of TiC_2, we first calculate the elastic constants to examine its mechanical stability. The elastic constants are calculated to be: C_{11} = 140.58 N/m, C_{22} = 70.52 N/m, C_{12} = 25.10 N/m, and C_{44} = 16.19 N/m. Obviously, they satisfy Born criteria,[54, 55] namely, C_{11}, C_{22}, C_{44} > 0 and $C_{11}C_{22}$ - C_{12}^2>0, suggesting that the TiC_2 sheet is mechanically stable. Based on the obtained elastic constants,[56] the Young's modulus $E(\theta)$ and Poisson's ratio $\nu(\theta)$ along an arbitrary in-plane direction θ (θ is the angle relative to the x direction) are calculated using the formula:[57]

$$E(\theta) = \frac{C_{11}C_{22} - C_{12}^2}{C_{11}s^4 + C_{22}c^4 + (\frac{C_{11}C_{22} - C_{12}^2}{C_{44}} - 2C_{12})c^2s^2} \quad (1)$$

$$v(\theta) = -\frac{(C_{11}+C_{22}-\frac{C_{11}C_{22}-C_{12}^2}{C_{44}})c^2s^2-C_{12}(s^4+c^4)}{C_{11}s^4+C_{22}c^4+(\frac{C_{11}C_{22}-C_{12}^2}{C_{44}}-2C_{12})c^2s^2} \quad (2)$$

where c = cos θ and s = sin θ. The results are plotted in Fig. 4. The deviations of E (θ) and ν (θ) from the perfect circles indicate the elastic anisotropy of the TiC_2 sheet, which results from the fact that all the C=C units are aligned parallel in the x direction. The Young's modulus in the x and y directions are found to be E_x = 131.17 N/m and E_y = 66.04 N/m, respectively. E_x is close to that of MXene Ti_2C (130 N/m).[42] In the y direction, Ti atoms bind to C_2 units through the interaction between Ti-3d and π orbitals of the C-C dimer. Because this interaction is weaker than the C=C bond, it results in a small value of E_y, being only half of E_x. Poisson's ratio is also a fundamental parameter describing the mechanical behavior of a material. For a perfectly incompressible and isotropic material, the Poisson's ratio is exactly equal to 0.5.[58] However, Fig. 4b shows that for the anisotropic TiC_2 sheet, the Poisson's ratio reaches 0.59 in some directions, which is much larger than that of MXene Ti_2C (0.23). For comparison, the main results of the elastic constants, Young's modulus, and Poisson's ratio of TiC_2 and other 2D layers are listed in Table 1.[56, 58-60]

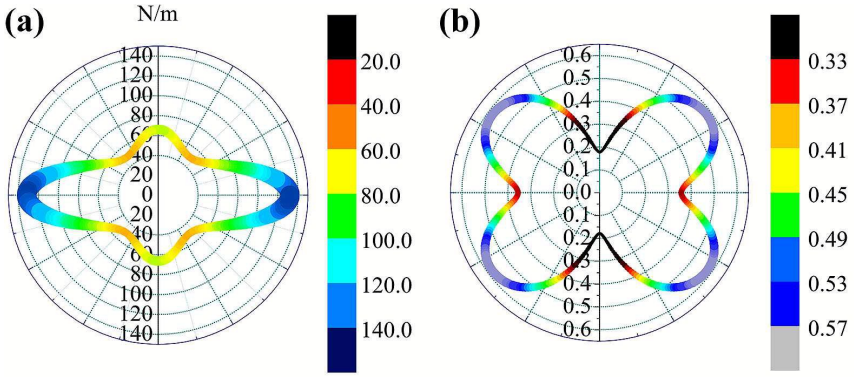

Fig. 4 Polar diagrams of (a) Young's modulus E (θ) and (b) Poisson's ratio v (θ) of the TiC_2 sheet.

Table 1. Elastic constants of C_{11} and C_{12}, in-plane Young's modulus Y, and Poisson's ratio *v* of the 2D TiC_2, Ti_2C, graphene, MoS_2, and *h*-BN sheets

Materials	elastic constants (N/m)		Y (N/m)	*v*
	C_{11}	C_{22}		
TiC_2	141	71	131(*x*) 61(*y*)	0.59(Max) 0.21(Min)
Ti_2C[42]	137	32	130	0.23
Graphene[59]	353	61	342	0.17
MoS_2[60]	140	40	129	0.31
h-BN[56]	335	89	318	0.27

4. Electronic properties

To study the electronic properties we calculate the electronic band structure of the TiC_2 sheet. The results are plotted in Fig. 5a. TiC_2 is found to be metallic as the partially occupied bands, namely the bands numbered as 12, 13, and 14, cross the Fermi level in the Brillouin zone. The metallicity is further confirmed by using the more accurate HSE06 functional.[61, 62] Orbital analysis suggests that the bands near the Fermi level are dominated by the Ti-3*d* orbitals, while the C-2*s* and 2*p* orbitals also make small contributions to the observed metallicity through hybridization with the Ti-3*d* states. We further calculate the band-decomposed charge densities and plot them in Fig. 5a as well. By carefully examining the charge distribution of each band, we clarify the interactions between the frontier orbitals of C_2 units and Ti atoms, as illustrated in Fig. 5b. The ground state electronic configuration of an isolated C_2 dimer is $(1\sigma_g)^2(1\sigma_u)^2(2\sigma_g)^2(2\sigma_u)^2(1\pi_u)^4$ with the higher states $(3\sigma_g)(1\pi_g)(3\sigma_u)$ unoccupied. The Ti atoms form a slightly distorted triangular sublattice, akin to that in recently predicted TiB_2.[63] The Ti-3*d* orbitals split into $e_1(d_{xy}, d_{xx-yy})$, $e_1^*(d_{xz}, d_{yz})$, and $a^*(d_{zz})$ in triangular crystal field. For comparison, we plot the energy bands formed by the sublattices of C_2 units and Ti atoms in Fig. S6, respectively.

In Fig. 5a, the 1st to 8th energy bands with energy ranging from -15 to -3.5 eV correspond to the $2\sigma_g$ (bonding), $2\sigma_u$ (anti-bonding), and π_u (bonding) states of the C_2 units, and lie deep

under the Fermi level because their energy are much lower than that of the Ti-3*d* states. The C_2-$3\sigma_g$ and π_g states hybridize with the Ti-3*d* and 4*s* states, forming the three fully occupied bands (the 9th, 10th, and 11th bands) and three partially occupied bands (the 12th, 13th, and 14th bands). The bands with energy higher than 2.0 eV are unoccupied and hence are not given in the band structure. To visualize the charge distribution, we plot the band-decomposed charge density isosurfaces for each individual band of the band structure in Fig. 5a, which clearly show the main contribution to the charge density of each band. For instance, the band-decomposed charge densities of the 9th and 10th bands mainly aggregate in the proximity of C_2, indicating that the C_2-$3\sigma_g$ orbitals are filled by the electrons of Ti donors in this 2D crystal. This is qualitatively consistent with our Bader charge analysis, which indicates that each Ti atom transfers about 1.5 electrons to each C_2 unit. The bands near the Fermi level are dominated by the Ti-3*d* states, and consequently the corresponding band-decomposed charge accumulates around the Ti atoms. The band-decomposed charge densities of the 11th and 12th bands clearly show the characteristics of Ti-3d_{xy} and 3d_{xz} orbitals, respectively, while both the 13th and 14th bands have the feature of Ti-3d_{zz} orbitals, indicating that the metallicity of TiC_2 originates from the electrons in Ti-3d_{xz} and 3d_{zz} orbitals. Interestingly, we note that the orbital interactions in TiC_2 are similar to those in bulk UC_2.[39] However, Ti-3*d* and 4*s* orbitals have much lower energy as compared to U-6*d*, which enables them to have stronger interaction with the frontier orbitals of C_2 units, leading to the stable 2D sheet.

We further discuss the influence of the occupation of C_2 orbitals on the C=C bond length. It has been demonstrated that in C_2 containing metal carbide systems, the more the C_2-π_u bonding orbital is occupied, or the less the C_2-π_g antibonding orbital is filled, the shorter is the C=C bond length.[39] The ground state of isolated C_2 has an equilibrium C-C distance of 1.31 Å. The reason that the C-C bond length (1.33 Å) in TiC_2 is slightly longer than that of an isolated C_2 dimer is because the C_2-π_g orbital is partially occupied.

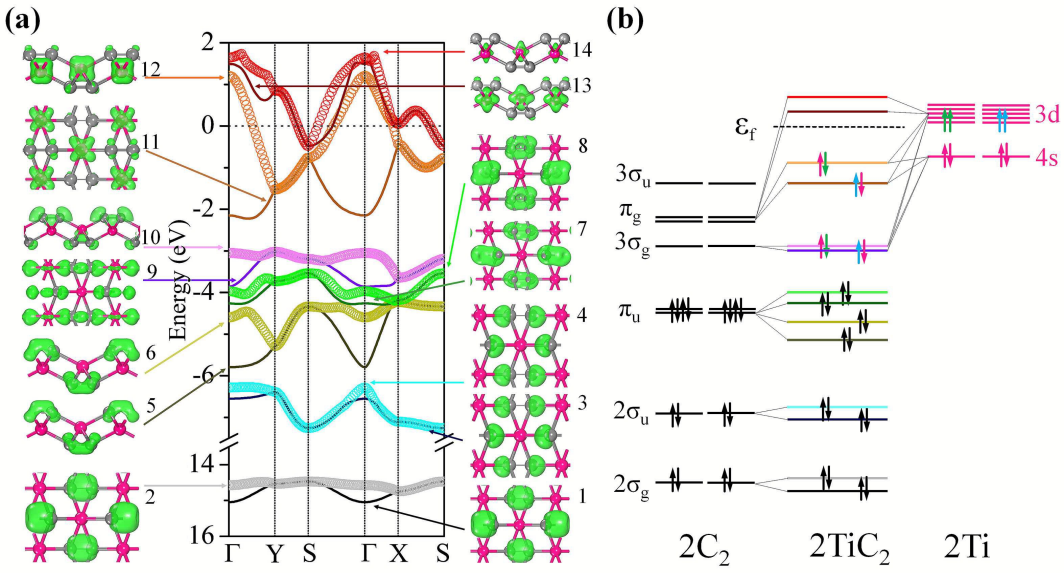

Fig. 5 (a) Electronic band structure, and decomposed charge density distributions (isovalue: 0.1 e/Å^3) for each band with the corresponding band index denoted of the TiC_2 sheet near the Fermi level. The Fermi energy is set to 0 eV. The high symmetry k point path is along: Γ (0, 0) → Y (0, 1/2) → S (1/2, 1/2) → Γ (0, 0) → X (1/2, 0) → S (1/2, 1/2). (b) Schematic diagram showing the interactions between the frontier orbitals of C_2 units and Ti atoms (Note that there are two C_2 units and two Ti atoms in a unit cell of TiC_2).

5. Potential application of TiC_2 as anode material in lithium ion battery

The metallicity of TiC_2 provides an intrinsic advantage in electrical conductivity as compared to semiconducting or insulating transition-metal oxides and TMDs layers. Therefore, it may find applications as electrodes. In fact, recently MXenes have been widely studied both theoretically and experimentally as promising anode materials for Li ion battery (LIB).[64, 65] Considering that TiC_2 possesses higher carbon content as compared to the MXene Ti_2C, we expect that this sheet can have a better Li storage capacity. In the following, we systematically explore the possibility of TiC_2 as a LIB anode material by looking at the adsorption and diffusion behaviors of Li atoms on this sheet, and derive the relative electrochemical properties of the Li adsorbed TiC_2.

To determine the preferable adsorption site of Li on the TiC_2 sheet, we use a 2×2 supercell and deposit one Li atom on different sites, corresponding to a stoichiometry of $Ti_8C_{16}Li$. Four typical adsorption configurations with high structural symmetry, labeled as C_I, C_{II}, C_{III} and C_{IV}, are considered, as shown in Fig. 6a, where C_I is the hollow site of the four neighboring carbon dimers, C_{II} is the on-top site of Ti that is in between the two neighboring C=C units lying along a line, C_{III} is the on-top site of Ti that is in between the two parallel C=C units lying in two neighboring lines, and C_{IV} is the bridge site of the C=C unit. Full geometry optimizations and total energy calculations are performed to identify their relative stability. C_I is found to be the lowest energy configuration with energy by 0.10, 0.15 and 0.72 eV respectively lower than that of C_{II}, C_{III} and C_{IV}, suggesting that Li atom prefers to occupy the hollow site of the carbon dimers on the TiC_2 sheet.

To evaluate the potential application of the TiC_2 sheet as an anode material for LIB, we investigate the possible diffusion paths of Li atom on this sheet and their corresponding energy barriers. We consider three trial diffusion paths that connect the two neighboring most preferable Li adsorption sites with high structural symmetry, as indicated in Fig. 6b. Pathway I is found to have the lowest diffusion barrier of 0.11 eV and the shortest diffusion length of 4.38 Å. The magnitude of energy barrier is even smaller than half of those of titanium carbides MXenes (see Table 2)[10, 64] implying a good conductivity of Li ions on the TiC_2 sheet, which is an important parameter for a LIB electrode material. When Li ions diffuse along path II (perpendicular to path I), the energy barrier is 0.16 eV. This is only 0.05 eV higher than that of path I. While the energy barrier is 0.76 eV when Li ions diffuse along path III, which is much larger than that of path I or path II. The variation of energy barrier with respect to the migration distance of Li on this sheet is plotted in Fig. 6c. Thus, it is clear that both path I and II are the possible routes for Li ion diffusion, which is beneficial for an electrode material.

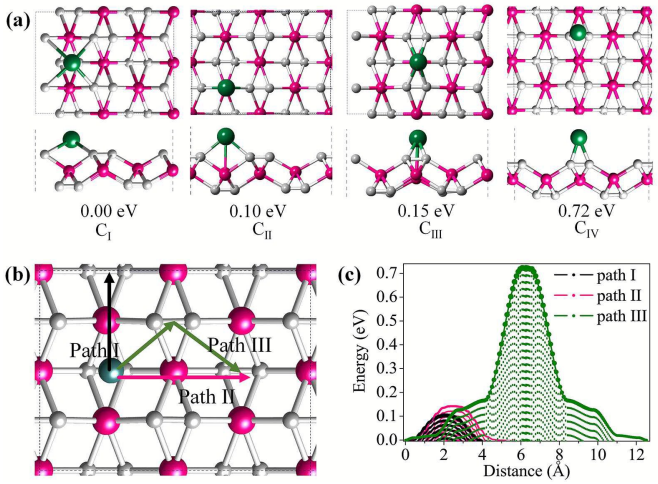

Fig. 6 (a) Four optimized configurations of the Li-adsorbed TiC_2 sheet ($Ti_8C_{16}Li$) and their relative energies with respect to the lowest energy configuration C_I. (b) Considered migration paths of Li diffusion on the TiC_2 sheet, and (c) the corresponding diffusion energy barrier profiles.

After investigating the adsorption site and the migration path, we study the adsorption of Li with high concentration. It has been demonstrated that the weight percentage of Li can reach 9% on the surfaces of the functionalized MXenes and multi-layer Li adsorption has been achieved, which significantly enhances the Li storage capacity.[64, 65] For the TiC_2 sheet, we first increase the concentration of Li from the stoichiometry of $Ti_8C_{16}Li$ to Ti_2C_4Li. The preferable adsorption site of Li is again determined to be the hollow site by following the same procedure mentioned in the above. Based on Bader charge analysis, we find that each adsorbed Li atom transfers 0.86 electrons to the TiC_2 sheet. We then calculate the phonon spectrum to examine the effect of Li adsorption on the dynamic stability of the TiC_2 sheet at such relatively high Li adsorption concentration. The calculated results are plotted in Fig. 7a, which shows that all the vibrational modes are real in the Brillouin zone, indicating that the adsorption of Li atom does not disturb the dynamic stability of the TiC_2 sheet. The total and

partial phonon DOS are then plotted in Fig. 7a as well, showing that the vibrations of the adsorbed Li atoms mainly contribute to the acoustic modes at the low frequency region.

To study the effect of high Li concentration on the electronic structure, we calculate the electronic band structure of the Ti_2C_4Li sheet and compare it with that of the pristine TiC_2 sheet. We note that the number of energy bands crossing the Fermi level increases upon Li adsorption, as shown in Fig. 7b, and the interaction between Li and Ti orbitals in the vicinity of the Fermi level is weak due to the repulsive interactions between the Ti and Li ions.

We further increase the concentration of Li by depositing a single layer of Li atoms on the both sides of the TiC_2 sheet, leading to a stoichiometry of TiC_2Li_2 (corresponding to a weight percentage of Li of 16.2%). Electrons over the Li layer form negatively charged cloud, same is the case with MXenes.[65] This is visualized by the calculated electron localization functions (ELF) (Fig. 7c). The average adsorption energy for each Li ion in this situation is 0.96 eV. We then introduce one more layer of Li atoms on both sides of the lithiated TiC_2 sheet, corresponding to a chemical ratio of TiC_2Li_4. The interaction between the two Li layers is visible from the calculated ELF shown in Fig. 7d, indicating that the second Li layer is able to bind with the lithiated TiC_2 sheet, as the negatively charged environment is favorable to the adsorption of the second Li layer. Here we see that the TiC_2 sheet has high Li storage capacity, this is very different from MXene Ti_2C sheet which needs surface functionalization for ion intercalation batteries.[65]

In the following, we calculate the average open circuit voltage (OCV) and the theoretical Li storage capacity, which are important electrochemical properties of an electrode material. OCV can be directly derived in a rather simple way:[66]

$$OCV \approx [E(TiC_2) + xE(Li) - E(TiC_2Li_x)]/x \qquad (3)$$

Here E (TiC_2), E (Li), and E (TiC_2Li_x) represent the free energies (total energy at 0 K) of pristine TiC_2, Li in bcc bulk, and the Li-adsorbed TiC_2, respectively. For the one layer

adsorption, the 2×2 supercell can accommodate up to 16 Li atoms, corresponding to a stoichiometry of TiC_2Li_2. The estimated OCV is 0.96 V, and the theoretical capacity is calculated to be 622 $mAh \cdot g^{-1}$. When the two-layer adsorption is considered, the stoichiometry is TiC_2Li_4. At such high Li concentration, the OCV and theoretical specific capacity are 0.29 V and 1226 $mAh \cdot g^{-1}$, respectively, showing that the new type TiC_2 sheet has much higher Li storage capacity as compared to previously reported $M_{n+1}C_n$ type of MXenes. For instance, the theoretical specific capacity of Ti_2C,[10] Ti_3C_2,[66] Nb_2C,[10] and V_2C[10] are 440 $mAh \cdot g^{-1}$, 320 $mAh \cdot g^{-1}$, 253 $mAh \cdot g^{-1}$, and 419 $mAh \cdot g^{-1}$, respectively. A comparison of our calculated specific capacity and diffusion barrier with several candidate anode materials for LIB are given in Table 2.[67-70] The high Li storage capacity of TiC_2 can be understood from the following facts: (i) when Li is adsorbed on the TiC_2 sheet, it transfers more electrons to the sheet (0.86 e) as compared to that of Li on MXenes,[66] resulting in a smaller radius of Li cation and a weaker Coulomb repulsion. (ii) The TiC_2 sheet has a higher carbon content than MXenes, thus has a higher specific capacity. (iii) TiC_2 has a lower mass areal density of 1.348 kg/m^2, which is much smaller than that of the MXene Ti_2C sheet (2.246kg/m^2).[42]

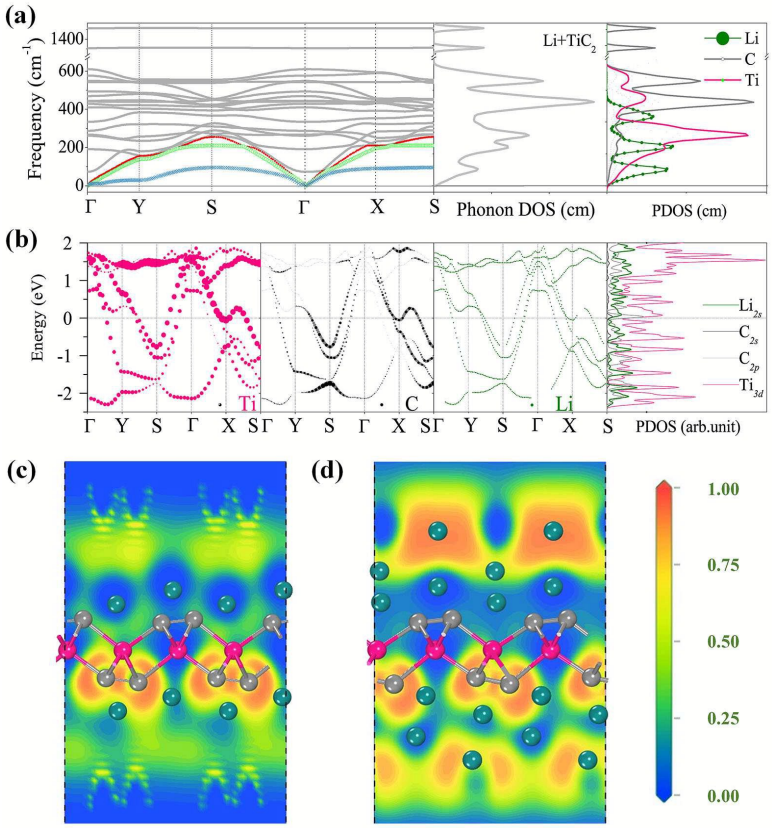

Fig. 7 (a) Phonon dispersion, phonon total and partial DOS, and (b) electronic band structure of Ti_2C_4Li. Bands compositions are indicated with size of circles. (c) and (d) ELF slices of the lithiated TiC_2 sheet with stoichiometry of TiC_2Li_2 and TiC_2Li_4, respectively.

Table 2. Comparison of specific capacity and diffusion barrier of candidate anode materials for Li ion battery. "-" means data unavailable.

Materials	Specific capacity (mAh/g)		Diffusion barrier (eV)		OCV (V)
	Theo.	Expt.	Theo.	Expt.	
TiC_2	622	-	0.11	-	0.96
Ti_2C	440[10]	-	0.27	-	0.44
Nb_2C	253[10]	-	-	-	0.52
V_2C	419[10]	-	-	-	0.47
Ti_3C_2	320[66]	-	0.07	-	0.62
f-Ti_3C_2	449[64]	410	0.28	-	-
Graphite	372	372	0.4[67]	-	0.2
TiO_2	200[68, 69]	200	-	0.35-0.65[70]	1.8

Conclusions

In conclusion, stimulated by the special role of C_2 dimer in the synthesis of many carbon-based materials as well as its special properties compared to individual C atoms, we have explored a new type of 2D transition metal carbide by taking the TiC_2 sheet as an example, which is composed of Ti centers and C=C dimers. Using state-of-the-art theoretical calculations, we demonstrated that this sheet is not only dynamically, mechanically and thermally stable, but also exhibits exceptional properties including metallic band structure, anisotropic elasticity, a large heat capacity and Debye stiffness. Due to its unique atomic configuration, the pristine TiC_2 sheet has outstanding Li storage capacity with a smaller migration energy barrier as compared with regular MXenes. In addition, compared to MXene Ti_2C sheets, TiC_2 has less exposed metal sites on the surfaces showing better chemical stability and lower mass density (only 60% of the Ti_2C sheet). In short, as a new member of the 2D metal carbide family, the studied TiC_2 sheet is unique as it contains C=C dimers instead of individual C atoms, and displays novel properties beyond MXenes.

Acknowledgements

This work is partially supported by grants from the National Natural Science Foundation of China (NSFC-11174014 and NSFC-51471004), the National Grand Fundamental Research 973 Program of China (Grant No. 2012CB921404), and the Doctoral Program of Higher Education of China (20130001110033). The calculations were carried out in Shanghai supercomputer center.

References

1. K. S. Novoselov, A. K. Geim, S. V. Morozov, D. Jiang, Y. Zhang, S. V. Dubonos, I. V. Grigorieva and A. A. Firsov, *Science*, 2004, **306**, 666-669.
2. Y. Li, L. Xu, H. Liu and Y. Li, *Chem. Soc. Rev.*, 2014, **43**, 2576-2582.
3. S. Zhang, J. Zhou, Q. Wang, X. Chen, Y. Kawazoe and P. Jena, *Proc. Natl. Acad. Sci.*, 2015, **112**, 2372-2377.
4. M. Naguib, M. Kurtoglu, V. Presser, J. Lu, J. Niu, M. Heon, L. Hultman, Y. Gogotsi and M. W. Barsoum, *Adv. Mater.*, 2011, **23**, 4248-4253.
5. M. Naguib and Y. Gogotsi, *Acc. Chem. Res.*, 2015, **48**, 128-135.
6. J.-C. Lei, X. Zhang and Z. Zhou, *Front. Phys.*, 2015, **10**, 276-286.
7. M. Kurtoglu, M. Naguib, Y. Gogotsi and M. W. Barsoum, *MRS Commun.*, 2012, **2**, 133-137.
8. M. Khazaei, M. Arai, T. Sasaki, C.-Y. Chung, N. S. Venkataramanan, M. Estili, Y. Sakka and Y. Kawazoe, *Adv. Funct. Mater.*, 2013, **23**, 2185-2192.
9. M. Naguib, V. N. Mochalin, M. W. Barsoum and Y. Gogotsi, *Adv. Mater.*, 2014, **26**, 992-1005.
10. C. Eames and M. S. Islam, *J. Am. Chem. Soc.*, 2014, **136**, 16270-16276.
11. F. Calvo, S. Diaz-Tendero and M. A. Lebeault, *Phys. Chem. Chem. Phys.*, 2009, **11**, 6345-6352.
12. Q. Wang, M.-F. Ng, S.-W. Yang, Y. Yang and Y. Chen, *ACS Nano*, 2010, **4**, 939-946.
13. M. Sternberg, P. Zapol and L. A. Curtiss, *Phys. Rev. B*, 2003, **68**, 205330.
14. L. Xu, Y. Jin, Z. Wu, Q. Yuan, Z. Jiang, Y. Ma and W. Huang, *J. Phys. Chem. C*, 2013, **117**, 2952-2958.
15. K. Bobrov, A. J. Mayne and G. Dujardin, *Nature*, 2001, **413**, 616-619.
16. B. C. Guo, K. P. Kerns and A. W. Castleman, *Science*, 1992, **255**, 1411-1413.
17. M.-M. Rohmer, M. Bénard and J.-M. Poblet, *Chem. Rev.*, 2000, **100**, 495-542.
18. N. J. Long and C. K. Williams, *Angew. Chem. Int. Ed.*, 2003, **42**, 2586-2617.
19. V. W.-W. Yam, *Acc. Chem. Res.*, 2002, **35**, 555-563.

20. T. P. Vaid, *J. Am .Chem. Soc.*, 2011, **133**, 15838-15841.
21. R. Buschbeck, P. J. Low and H. Lang, *Coordin. Chem. Rev.*, 2011, **255**, 241-272.
22. A. L. Ivanovskii, A. A. Sofronov and Y. N. Makurin, *Theo. Exp. Chem.*, 1999, **35**, 270-274.
23. B. C. Guo, S. Wei, J. Purnell, S. Buzza and A. W. Castleman, *Science*, 1992, **256**, 515-516.
24. S. Wei, B. C. Guo, J. Purnell, S. Buzza and A. W. Castleman, *Science*, 1992, **256**, 818-820.
25. J.-O. Joswig and M. Springborg, *J. Chem. Phys.*, 2008, **129**, 134311.
26. A. T. Paxton and C. Elsässer, *Phys. Rev. B*, 2013, **87**, 224110.
27. G. Kresse and J. Furthmüller, *Phys. Rev. B*, 1996, **54**, 11169-11186.
28. Z. Zhang, X. Liu, B. I. Yakobson and W. Guo, *J. Am. Chem. Soc.*, 2012, **134**, 19326-19329.
29. P. E. Blöchl, *Phys. Rev. B*, 1994, **50**, 17953-17979.
30. J. P. Perdew, K. Burke and M. Ernzerhof, *Phys. Rev. Lett.*, 1996, **77**, 3865-3868.
31. H. J. Monkhorst and J. D. Pack, *Phys. Rev. B*, 1976, **13**, 5188-5192.
32. A. Togo, F. Oba and I. Tanaka, *Phys. Rev. B*, 2008, **78**, 134106.
33. S. Nosé, *J. Chem. Phys.*, 1984, **81**, 511-519.
34. W. Tang, E. Sanville and G. Henkelman, *J. Phys.: Condens. Matter*, 2009, **21**, 084204.
35. G. Mills and H. Jónsson, *Phys. Rev. Lett.*, 1994, **72**, 1124-1127.
36. M.-M. Rohmer, M. Benard, C. Henriet, C. Bo and J.-M. Poblet, *J. Chem. Soc. Chem. Commun.*, 1993, 1182-1185.
37. X. Zhang, Z. Ma, X. Zhao, Q. Tang and Z. Zhou, *J. Mater. Chem. A*, 2015, **3**, 4960-4966.
38. M. Naguib, O. Mashtalir, J. Carle, V. Presser, J. Lu, L. Hultman, Y. Gogotsi and M. W. Barsoum, *ACS Nano*, 2012, **6**, 1322-1331.
39. J. Li and R. Hoffmann, *Chem. Mater.*, 1989, **1**, 83-101.
40. R. Sumathi and M. Hendrickx, *Chem. Phys. Lett.*, 1998, **287**, 496-502.

41. C. Berkdemir, A. W. Castleman and J. O. Sofo, *Phys. Chem. Chem. Phys.*, 2012, **14**, 9642-9653.

42. S. Wang, J.-X. Li, Y.-L. Du and C. Cui, *Comp. Mater. Sci.*, 2014, **83**, 290-293.

43. M. A. Sobhy, A. W. Castleman and J. O. Sofo, *J. Chem. Phys.*, 2005, **123**, 154106.

44. J. I. Martinez, A. Castro, A. Rubio and J. A. Alonso, *J. Chem. Phys.*, 2006, **125**, 074311.

45. G. K. Gueorguiev and J. M. Pacheco, *Phys. Rev. Lett.*, 2002, **88**, 115504.

46. J. Tersoff and D. R. Hamann, *Phys. Rev. B*, 1985, **31**, 805-813.

47. S. Mogck, B. J. Kooi, J. T. M. De Hosson and M. W. Finnis, *Phys. Rev. B*, 2004, **70**, 245427.

48. J. C. Meyer, S. Kurasch, H. J. Park, V. Skakalova, D. Künzel, A. Groß, A. Chuvilin, G. Algara-Siller, S. Roth, T. Iwasaki, U. Starke, J. H. Smet and U. Kaiser, *Nat. Mater.*, 2011, **10**, 209-215.

49. L. Wu, Y. Zhu, T. Vogt, H. Su, J. W. Davenport and J. Tafto, *Phys. Rev. B*, 2004, **69**, 064501.

50. W. Li and N. Mingo, *Phys. Rev. B*, 2014, **90**, 094302.

51. S. Zhang, Q. Wang, X. Chen and P. Jena, *Proc. Natl. Acad. Sci.*, 2013, **110**, 18809-18813.

52. P. Liu, J. A. Rodriguez, H. Hou and J. T. Muckerman, *J. Chem. Phys.*, 2003, **118**, 7737-7740.

53. T. Tohei, A. Kuwabara, F. Oba and I. Tanaka, *Phys. Rev. B*, 2006, **73**, 064304.

54. K.Huang, M.Born, *Clarendon,Oxford*, 1954.

55. J. Wang, S. Yip, S. R. Phillpot and D. Wolf, *Phys. Rev. Lett.*, 1993, **71**, 4182-4185.

56. K. H. Michel and B. Verberck, *Phys. Rev. B*, 2009, **80**, 224301.

57. E. Cadelano, P. L. Palla, S. Giordano and L. Colombo, *Phys. Rev. B*, 2010, **82**, 235414.

58. G. N. Greaves, A. L. Greer, R. S. Lakes and T. Rouxel, *Nat. Mater.*, 2011, **10**, 823-837.

59. R. C. Andrew, R. E. Mapasha, A. M. Ukpong and N. Chetty, *Phys. Rev. B*, 2012, **85**, 125428.

60. R. C. Cooper, C. Lee, C. A. Marianetti, X. Wei, J. Hone and J. W. Kysar, *Phys. Rev. B*, 2013, **87**, 035423.

61. J. Heyd, G. E. Scuseria and M. Ernzerhof, *J. Chem. Phys.*, 2003, **118**, 8207-8215.

62. J. Heyd, G. E. Scuseria and M. Ernzerhof, *J. Chem. Phys.*, 2006, **124**, 219906.

63. L. Z. Zhang, Z. F. Wang, S. X. Du, H. J. Gao and F. Liu, *Phys. Rev. B*, 2014, **90**, 161402.

64. Y. Xie, M. Naguib, V. N. Mochalin, M. W. Barsoum, Y. Gogotsi, X. Yu, K.-W. Nam, X.-Q. Yang, A. I. Kolesnikov and P. R. C. Kent, *J. Am. Chem. Soc.*, 2014, **136**, 6385-6394.

65. Y. Xie, Y. Dall'Agnese, M. Naguib, Y. Gogotsi, M. W. Barsoum, H. L. Zhuang and P. R. C. Kent, *ACS Nano*, 2014, **8**, 9606-9615.

66. Q. Tang, Z. Zhou and P. Shen, *J. Am. Chem. Soc.*, 2012, **134**, 16909-16916.

67. K. Persson, V. A. Sethuraman, L. J. Hardwick, Y. Hinuma, Y. S. Meng, A. van der Ven, V. Srinivasan, R. Kostecki and G. Ceder, *J. Phys. Chem. Lett.*, 2010, **1**, 1176-1180.

68. M. V. Koudriachova, N. M. Harrison and S. W. de Leeuw, *Solid State Ionics*, 2002, **152-153**, 189-194.

69. M. V. Koudriachova, N. M. Harrison and S. W. de Leeuw, *Solid State Ionics*, 2003, **157**, 35-38.

70. C. H. Sun, X. H. Yang, J. S. Chen, Z. Li, X. W. Lou, C. Li, S. C. Smith, G. Q. Lu and H. G. Yang, *Chem. Commun.*, 2010, **46**, 6129-6131.